Progress in Additive Manufacturing
https://doi.org/10.1007/s40964-026-01992-2

RESEARCH

3D-printed spacers integrated with module vibration for enhanced ultrafiltration permeability and antifouling

Aws N. Al-Tayawi[1,2] · Noor Al-Hammadi[3] · Omar K. Mohialdeen[3] · Imre Vajk Fazekas[1] · Bence Szilveszter Virág[1] · Judit Kopniczky[1] · Tamás Gyulavári[1] · Zsuzsanna László[1] · Szabolcs Kertész[1]

Received: 16 July 2026 / Accepted: 16 September 2026

Abstract

The incorporation of 3D-printed spacers into membrane filtration systems has recently emerged as a promising strategy for enhancing filtration performance and mitigating membrane fouling. This study integrated four 3D-printed spacer designs into a vibratory cross-flow ultrafiltration system to evaluate their combined effect with module vibration on dairy wastewater treatment. System performance was assessed using key indicators, including permeate flux, *COD* retention, total membrane resistance, and specific energy consumption. Results showed that *PETG*-based spacers, particularly the conical design, increased permeate flux by up to 300% relative to the control, with fourfold flux enhancements achieved when combined with module vibration. *COD* retention improved modestly across most configurations, while total resistance was consistently reduced by approximately 76 to 85% relative to the control, with the greatest decrease observed for the conical spacer under high-vibration conditions. Energy analysis further confirmed that combining 3D-printed spacers with module vibration was the most efficient operating strategy, markedly lowering specific energy consumption relative to the control. Overall, the conical and reinforced branched spacer designs operated under high vibration achieved the best overall balance of flux enhancement, resistance reduction, and energy efficiency, highlighting their potential for sustainable, low-fouling ultrafiltration applications.

Keywords 3D printed spacer · Dairy wastewater · Membrane fouling mitigation · Ultrafiltration

List of symbols

J	The permeate flux $[\mathrm{L \cdot m^{-2} \cdot h^{-1}}]$
V	The permeate volume $[\mathrm{m^3}]$
A	Active surface of the membrane $[\mathrm{m^2}]$
t	Filtration time [s]
R	Retention value [%]
c_P	Concentration of the permeate [mg/L]
c_F	Concentration of the feed [mg/L]
R_T	Total resistance [1/m]
R_{IRR}	Irreversible resistance [1/m]
R_{REV}	Reversible resistance [1/m]
TMP	Transmembrane pressure [Pa]

✉ Aws N. Al-Tayawi
awsaltayawi@uomosul.edu.iq

✉ Szabolcs Kertész
kertesz@mk.u-szeged.hu

Noor Al-Hammadi
noorabdalkany@uomosul.edu.iq

Omar K. Mohialdeen
omar.k.aldeen@uomosul.edu.iq

Imre Vajk Fazekas
fazekasimi@yahoo.com

Bence Szilveszter Virág
szilvesztervirag2@gmail.com

Judit Kopniczky
jkopniczky@titan.physx.u-szeged.hu

Tamás Gyulavári
gyulavarit@chem.u-szeged.hu

Zsuzsanna László
zsizsu@mk.u-szeged.hu

1 University of Szeged, Szeged, Hungary

2 University of Mosul, Mosul, Iraq

3 University of Mosul, Mosul, Iraq

Published online: 24 September 2026

J_{W1}	Water flux of the pristine membrane [L m^{-2} h^{-1}]
J_{W2}	Water flux of the membrane after wastewater experiment and polarization layer removing [L m^{-2} h^{-1}]
η_w	The dynamic viscosity of water at 25°C [Pas]
η_{ww}	The dynamic viscosity of wastewater at 25°C [Pas]
V_F	The initial volume of the feed [m^3]
V_P	The permeate volume [m^3]
SE	Specific energy consumption [kWh/m^3]
η_{FP}	Efficiency of the feed pump [-]
η_{VM}	Efficiency of the vibration motor in case of module vibration [-]
P_{FP}	Power of the feed pump [kW]
P_{VM}	Power of the vibration motor in case of module vibration [kW]

1 Introduction

Pressure-driven membrane filtration processes play a vital role in potable water production and wastewater treatment, thereby contributing to the mitigation of global water scarcity [19, 35]. The sustainable operation of these systems depends on reducing energy consumption and extending membrane lifespan [8, 24, 27]. However, membrane fouling remains a major challenge, as it inevitably impairs filtration performance [21, 31]. Fouling is caused by the accumulation of undesirable substances on the membrane surface and within membrane pores as a result of complex physicochemical interactions [11, 23]. Consequently, a substantial decline in water flux is often observed, which, unless offset by an increase in transmembrane pressure, leads to higher energy consumption [6, 7].

To mitigate membrane fouling, considerable attention has been directed toward hydrodynamic strategies, which have emerged as an effective alternative to chemical-based cleaning approaches. By modifying feed-flow characteristics near the membrane surface, these strategies can reduce foulant deposition and improve filtration performance [5, 18, 33]. Recent developments in additive manufacturing (3D printing) have further enhanced opportunities for hydrodynamic optimization by enabling the fabrication of complex spacer geometries that are difficult to achieve using conventional manufacturing techniques. This capability has accelerated the development of a wide range of 3D-printed spacer (*3DPS*) configurations [3, 25, 32]. *3DPS* structures function as turbulence promoters, altering local flow patterns and enhancing fluid mixing in the vicinity of the membrane surface [1, 12, 13]. The resulting increase in local shear stress weakens foulant adhesion and limits their accumulation on the membrane surface. At the same time, enhanced mixing mitigates concentration polarization by promoting the back transport of solutes from the membrane surface to the bulk solution, thereby reducing the formation of concentrated boundary layers that often initiate fouling. Consequently, mass transfer is improved, and cake layer development is significantly suppressed [15]. In addition, optimized spacer geometries can generate localized vortices and recirculation zones that further improve mixing while reducing stagnant, low-velocity regions where foulants typically accumulate [13, 32]. These flow modifications also promote a more uniform shear stress distribution across the membrane surface, minimizing fouling-prone regions around spacer filaments and inhibiting biofilm growth. Collectively, these effects contribute to enhanced membrane cleanliness, improved operational stability, and prolonged filtration performance [12].

On the other hand, the Vibratory Shear Enhanced Process (*VSEP*) has demonstrated remarkable effectiveness in treating liquids with a high fouling potential, including highly concentrated whey and industrial effluents containing elevated concentrations of suspended and dissolved solids [7, 34, 36]. This membrane-based separation technology employs high-frequency vibrations to generate shear forces at the membrane surface, thereby reducing foulant deposition and sustaining filtration performance [10, 36]. Despite its advantages in fouling control, *VSEP* systems typically require higher energy consumption than conventional membrane filtration systems, primarily due to the continuous operation of the mechanical vibration mechanism [4, 30]. The integration of *3DPS* into *VSEP* systems has shown considerable potential for enhancing membrane performance, mitigating fouling and reduce energy consumption, particularly in wastewater ultrafiltration applications. Kertész [14] reported that star-shaped and column-shaped spacer geometries significantly improved system efficiency compared with the control configuration without spacers. These improvements were attributed to the optimization of flow dynamics within the *VSEP* unit, which enhanced mass transport and overall treatment performance [14]. The importance of spacer geometry in membrane processes has also been demonstrated by Cabrera-Castillo et al. [3], who found that gyroid-shaped spacers in membrane distillation systems promoted high water recovery while simultaneously reducing membrane fouling under conditions of elevated organic loading [3]. These findings suggest that geometrically optimized *3DPS* may similarly reduce fouling in *VSEP* systems by promoting more uniform flow distribution and minimizing foulant accumulation.

Membrane filtration performance is generally evaluated using a combination of indicators that reflect productivity, separation efficiency, fouling behavior, and energy consumption. Among these, permeate flux is one of the most commonly used measures of filtration productivity [26, 29], while retention or rejection provides an indication of the separation efficiency and contaminant removal achieved by the membrane [20]. However, flux and rejection alone do not provide sufficient information about the extent or nature of membrane fouling. For this reason, the resistance-in-series approach is often used to separate the overall filtration resistance into membrane resistance and reversible and irreversible fouling components providing a clearer understanding of fouling development and its reversibility [22, 28]. In addition, specific energy consumption (SEC) has become an important indicator for assessing the energy efficiency of membrane processes, as it relates the energy required for operation to the volume of permeate produced and allows the energy performance of different filtration configurations to be compared [2, 17]

This study investigates strategies for mitigating membrane fouling and ensuring the long-term efficiency of filtration processes. The primary objective is to examine mechanical methods for fouling reduction, with an emphasis on environmental sustainability, through the use of *3DPS* designed with different geometries, in conjunction with module vibration. Although hydrodynamic spacer design has been shown to enhance membrane filtration performance through flow modification and fouling mitigation, and module vibration has been shown to improve mass transfer and reduce concentration polarization and fouling independently, these approaches have predominantly been investigated as separate hydrodynamic strategies. Consequently, their combined effects within a vibratory cross-flow membrane system remain insufficiently understood. In particular, it remains unclear whether the flow perturbations induced by spacer geometry interact synergistically with vibration-induced shear forces, resulting in enhanced fouling control and filtration performance beyond the effects of either strategy alone, or whether their contributions are primarily additive. The novelty of the present study lies in its investigation of the coupled effects of spacer geometry and module vibration within a single vibratory cross-flow filtration system. To address this, four spacer geometries were purposefully designed to isolate distinct flow-modification mechanisms: the cylindrical spacer served as a baseline turbulence promoter, using evenly spaced pillars to disrupt the boundary layer and induce localized mixing; the conical spacer introduced a tapering profile to accelerate and redirect feed flow toward the membrane surface, intensifying local shear stress and more effectively suppressing concentration polarization; the branched spacer employed bifurcating channels to distribute flow more evenly across the membrane, reducing the stagnant, low-velocity zones where foulants typically accumulate; and the reinforced branched spacer extended this branched design with additional structural supports at the junctions, sustaining favorable flow distribution while withstanding the cyclic mechanical stresses imposed by vibration. By evaluating these geometries individually and in combination with vibration, the study compares key performance parameters, including membrane retention, permeate flux, specific energy consumption, and membrane resistance, to determine which geometric principles most effectively complement module vibration in enhancing filtration performance while minimizing energy demand.

Table 1 Analytical characteristics of the model wastewater

Parameter	Value
pH	8.5 ± 0.2
Turbidity [NTU]	1100 ± 25
Conductivity [μS/cm]	850 ± 10
Chemical oxygen demand [mg/L]	4800 ± 200
Total dissolved solids [ppm]	420 ± 20

2 Materials and methods

2.1 Model dairy westwater preparation

Model dairy effluent was generated to simulate a typical medium-strength effluent under controlled laboratory conditions. The effluent was prepared by dissolving 50 g/L of skimmed milk powder (Tutti Kft., Hungary) and 5 g/L of anionic detergent (CHEMIPUR CL 80) in 10 litters of tap water at ambient temperature. The solution was homogenized for a minimum of 30 min using a laboratory-grade four-arm mechanical mixer operating at 400 rpm. A constant temperature of 25 ± 1 °C was maintained for the model wastewater during the experiments by means of the integrated cooling circuit. The average properties of the model wastewater are summarized in Table 1.

2.2 Fabrication and characterization of 3D printed spacers

Four spacer designs, cylindrical (Sp.1), conical (Sp.2), branched (Sp.3), and reinforced branched (Sp.4), were fabricated by fused deposition modeling (FDM) using polyethylene terephthalate glycol (PETG) filament, with each geometry developed from distinct fluid dynamic principles rather than as arbitrary structural variants, together with our previous experience in membrane filtration (Fig. 1). The cylindrical spacer served as a baseline turbulence promoter, using evenly spaced pillars to disrupt the boundary layer and induce localized mixing. The conical spacer introduced a tapering profile to accelerate and redirect feed flow toward the membrane surface, intensifying local shear stress and more effectively suppressing concentration polarization. The branched spacer employed bifurcating channels to

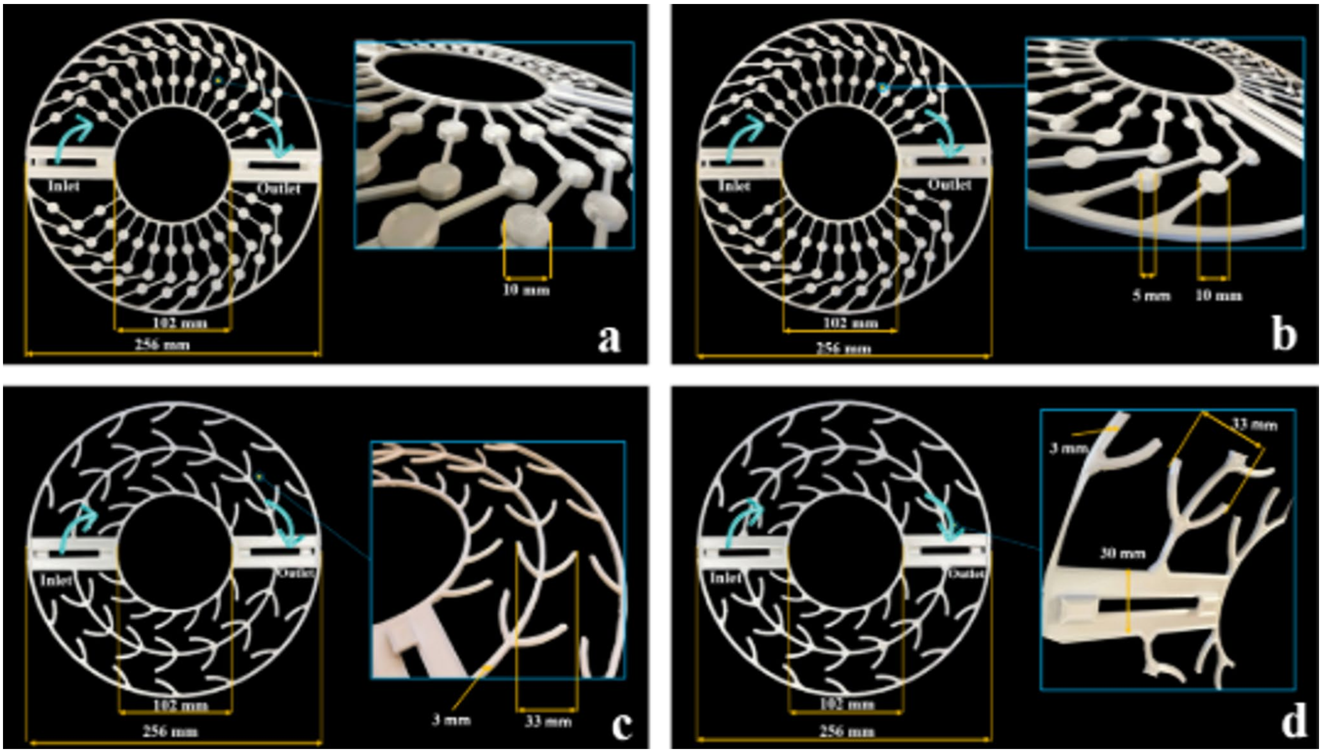

Fig. 1 Geometric configuration of the four *3DPS* evaluated in this study: **A** cylindrical, **B** conical, **C** branched, and **D** reinforced branched designs, illustrating the progressive structural modifications introduced to optimize flow distribution and mechanical durability

distribute flow more evenly across the membrane, reducing the stagnant, low-velocity zones where foulants typically accumulate. The reinforced branched spacer extended this branched design with additional structural supports at the junctions, sustaining favorable flow distribution while withstanding the cyclic mechanical stresses imposed by vibration, a demand that conventional, static spacer applications do not impose. Progressing from a simple pillar arrangement to increasingly elaborate flow-distribution and reinforcement strategies allowed each design iteration to be evaluated against the last, isolating which geometric features most effectively translate into filtration gains once vibration is introduced.

The use of 3D printing enabled rapid prototyping and iterative refinement of the spacer designs based on experimental feedback. A CR-10S Pro V2 3D printer (Creality, China) was used for spacer fabrication, offering a build volume of 300 × 300 × 400 mm and equipped with a BL-Touch automatic bed-leveling sensor to ensure consistent first-layer adhesion. Standard 1.75 mm filament was extruded through a heated nozzle (up to 260 °C), with layer heights ranging from 100 to 400 µm. Slicing was performed using Ultimaker Cura v5.7.0 (Ultimaker, Netherlands). Three-dimensional surface plots and visual data analyses were generated using TIBCO Statistica (v14.0.1.25, TIBCO Software Inc., USA) for performance evaluation and interpretation.

2.3 Ultrafiltration system and experimental setup

All membrane filtration experiments were conducted using a *VSEP* Series L modular vibratory membrane system Fig. 2. This system was equipped with a closed-loop, air-conditioned coolant circulation unit (capacity: 300 L), which maintained a constant operational temperature of 25 ± 1 °C through indirect wall cooling, thereby mitigating thermal accumulation during prolonged runs. The vibration amplitude of the system was adjustable between 0.635 cm and 2.54 cm by varying the vibration motor frequency. For clarity, these amplitudes are hereafter referred to as low (0.635 cm) and high (2.54 cm) vibration levels. A commercial polyether sulfone (*PES*) ultrafiltration membrane with a molecular weight cut-off (*MWCO*) of 30 kDa was employed in all trials. Selected experiments included the integration of the *3DPS* between the membrane surface and the module base to assess their influence on filtration performance. Filtration was carried out at a constant transmembrane pressure (TMP) of 0.8 MPa and a cross-flow rate of 15.14 L/min. Each run commenced with a homogenized 10 L batch of model wastewater, continuously recirculated via a feed pump. Separation of permeate and retentate followed cross-flow principles, with the retentate stream recycled back into the feed tank and the permeate collected in a separate vessel. Real-time permeate volume was recorded, and permeate

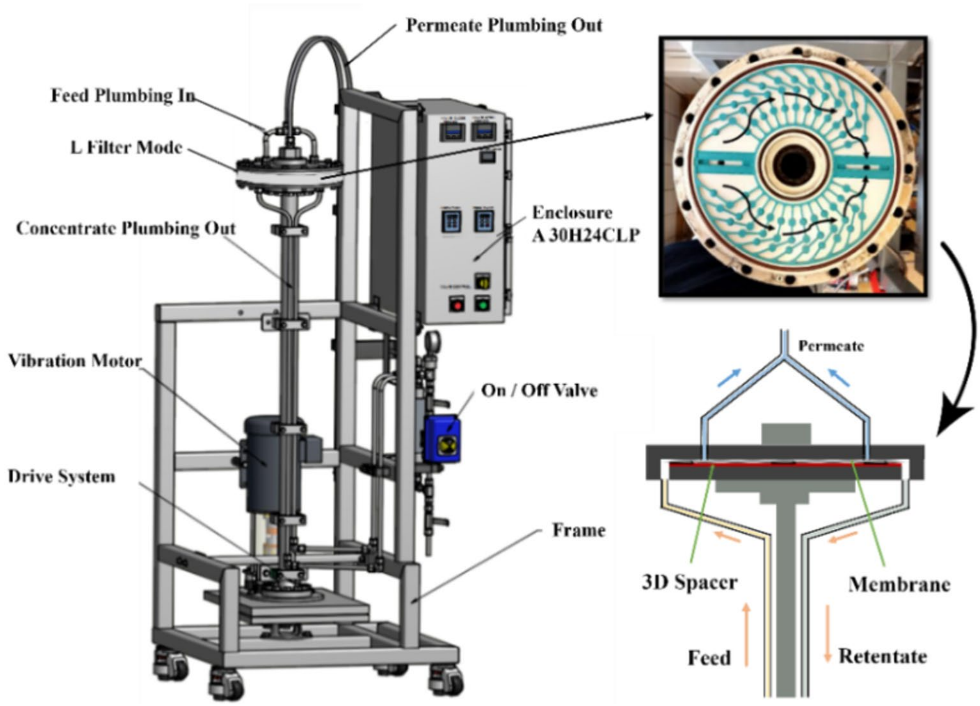

Fig. 2 Schematic representation of the VSEP Series L vibratory membrane filtration system and membrane module with the integrated 3D-printed spacer

flux was calculated accordingly. Each experiment was terminated upon reaching either a fivefold concentration factor (approximately 8 L permeate, accounting for a system dead volume of 1.5 L) or a maximum operational duration of 120 min, beyond which the permeate flux typically stabilized.

2.4 Surface morphology and topography analysis

Membrane surface morphology was examined using a cold field emission scanning electron microscope (*SEM*) (Hitachi S-4700 Type II, Japan) operated at an accelerating voltage of 10 kV with a secondary electron detector, conditions selected to enhance surface sensitivity while minimizing electron-beam damage to the polymeric membranes. Only surface topography was assessed, with no elemental or chemical composition analysis performed. Prior to imaging, membrane samples were cut to size, mounted on aluminum stubs using double-sided conductive carbon tape, and sputter-coated with a thin gold layer (~ 5 nm) under low pressure to enhance conductivity and prevent surface charging. Images were captured at multiple magnifications to characterize surface and pore structure and to qualitatively assess morphological differences between pristine and fouled/spacer-assisted membranes indicative of fouling. Surface topography and roughness were further evaluated using atomic force microscopy (*AFM*) (PSIA XE-100, South Korea) operated in non-contact mode. All samples were scanned in air under ambient conditions over a $10 \times 10\ \mu m^2$ scan area, enabling qualitative and quantitative comparison of surface roughness among the pristine, fouled, and spacer-assisted membranes.

2.5 Analytical methods

To evaluate membrane performance and characterize the filtration process, multiple analytical measurements were performed, including the determination of turbidity, electrical conductivity, pH, total dissolved solids (*TDS*), chemical oxygen demand (*COD*), and key milk constituents such as lactose, protein, and total dry matter. Samples were collected from the initial feed (original fluid), permeate, and retentate streams. Turbidity was measured using a nephelometric method with a turbidimeter (Model 2100AN; HACH, USA). Electrical conductivity and TDS were simultaneously measured using a portable conductivity meter (Model AD31; ADWA Instruments, Hungary), while pH was determined using a calibrated analytical multimeter (ADWA Instruments, Hungary). *COD* was assessed through oxidative digestion followed by photometric analysis; specifically, 200 µL samples were added to high-range (15,000 mg/L) potassium dichromate test tubes and digested at 150 °C for 120 min using a thermal reactor (Model ET 108; Lovibond, Belgium), with absorbance measured by a Lovibond spectrophotometer against a contaminant-free distilled water blank. Finally, quantification of lactose, protein, and total dry matter was conducted via mid-infrared spectroscopy using a Bentley 150 infrared spectrophotometer (Bentley Instruments Inc., USA), exploiting characteristic absorption bands for accurate constituent identification and quantification.

2.6 Key parameters and performance indicators

In membrane filtration, performance is commonly evaluated by determining the permeate flux, defined as the volume or mass of liquid filtered through a unit membrane area over a given time. This parameter, also termed volumetric or mass flow density [16]. In the present study, filtration performance was assessed based on the permeate flux, which was determined from the volume of permeate collected over a known filtration period and normalized to the active membrane area, as described by Eq. (1). The calculation assumes that the effective membrane area remains unchanged throughout the experiment. All filtration experiments were conducted under controlled operating conditions, with the temperature maintained at 25±1 °C, the transmembrane pressure (TMP) maintained at 0.8 MPa, and the cross-flow rate maintained at 15.14 L/min. The feed was continuously recirculated throughout each experiment to ensure consistent hydrodynamic conditions within the filtration module. Potential sources of experimental variability included the measurement of permeate volume and filtration time, small fluctuations in temperature and TMP, membrane-to-membrane variability, and the progressive change in feed concentration during filtration. These sources of variability were minimized by maintaining controlled operating conditions and following the same experimental procedure for all tested configurations.

$$J = \frac{V}{t \cdot A} \left[\mathrm{L} \cdot m^{-2} \cdot h^{-1}\right] \tag{1}$$

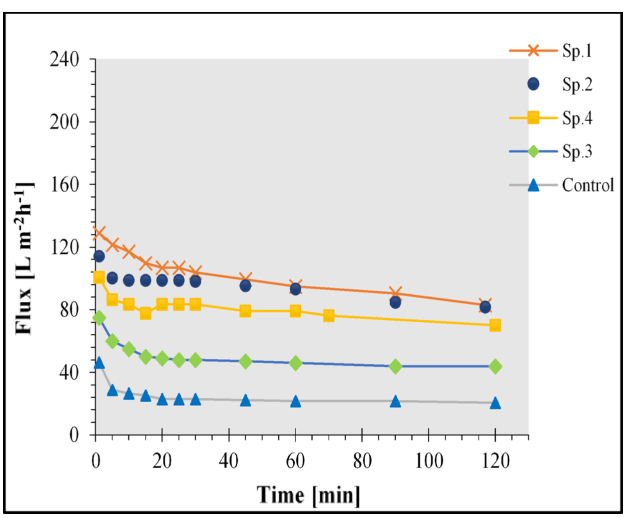

Fig. 3 Time-dependent permeate flux profiles obtained over a 120 min filtration run for the control (without spacer) and each *3DPS* design (Sp.1-Sp.4), illustrating the influence of spacer geometry on flux decline in the absence of vibration

Membrane retention (*R*) was quantified for COD, turbidity, and conductivity using Eq. (2):

$$R = \left(1 - \frac{C_P}{C_F}\right) \cdot 100 \qquad [\%] \tag{2}$$

Membrane resistance was further examined to characterize both the extent and nature of fouling, as well as the membrane's susceptibility to it. Within the resistance-in-series model, permeate flux is inversely proportional to total resistance, which in turn governs fouling behavior, operational stability, and membrane longevity. Total resistance (Eq. 3) was calculated as the sum of the intrinsic membrane resistance (Eq. 4), irreversible fouling resistance (Eq. 5), and reversible fouling resistance (Eq. 6):

$$R_T = R_M + R_{\mathrm{IRR}} + R_{\mathrm{REV}} \qquad \left[\mathrm{m}^{-1}\right] \tag{3}$$

$$R_M = \frac{\mathrm{TMP}}{J_{\mathrm{W1}} \cdot \eta_W} \qquad \left[\mathrm{m}^{-1}\right] \tag{4}$$

$$R_{\mathrm{IRR}} = \frac{\mathrm{TMP}}{J_{\mathrm{W2}} \cdot \eta_W} - R_M \qquad \left[\mathrm{m}^{-1}\right] \tag{5}$$

$$R_{\mathrm{REV}} = \frac{\mathrm{TMP}}{J_C \cdot \eta_{\mathrm{WW}}} - R_M - R_{\mathrm{IRR}} \qquad \left[\mathrm{m}^{-1}\right] \tag{6}$$

Specific energy consumption (*SEC*) was calculated using the permeate flux, membrane active surface area, and the power and efficiency of the vibration motor and the feed pump, as shown in Eq. (7).

$$\mathrm{SE} = \frac{\eta_{\mathrm{FP}} \cdot P_{\mathrm{FP}} + \eta_{\mathrm{VM}} \cdot P_{\mathrm{VM}}}{J \cdot A} \qquad \left[\mathrm{kWh/m^3}\right] \tag{7}$$

3 Results and discussions

3.1 Evaluation of membrane filtration fluxes

Membrane filtration efficiency was assessed through measurements of permeate flux. As shown in Fig. 3, the integration of *3DPS* enhanced permeate flux in all cases relative to the control (without spacer), even in the absence of vibration. Designs Sp.1 and Sp.2 exhibited the greatest improvements, with Sp.1 nearly tripling the control flux. This result is consistent with the underlying mechanism of the cylindrical spacer, whose evenly spaced pillars disrupt the boundary layer along the entire membrane length, sustaining a continuous turbulent regime that limits foulant deposition across the surface. Sp.2 achieved a flux only 12% lower than Sp.1, despite relying on a markedly different mechanism: rather than promoting turbulence uniformly, its tapered profile accelerates and redirects flow toward specific regions of the membrane, concentrating shear stress where it is most needed. The comparable performance of this more localized approach indicates that concentrated, high-intensity shear can rival the effect of broadly distributed turbulence in mitigating fouling. Sp.3 produced the smallest improvement among the tested designs, though its 47% increase in flux relative to the control remains substantial. Its bifurcating channel geometry effectively redistributes flow and minimizes stagnant regions prone to foulant accumulation; however, in the absence of a strong flow-accelerating or turbulence-promoting element, the resulting shear stress at the membrane surface is comparatively lower than that generated by Sp.1 or Sp.2. These findings are consistent with those of Gáspár and Neczpál [9], who reported that optimized flow baffle geometries could enhance initial flux by up to 500% through a combination of fouling mitigation and flow redistribution.

Integrating *3DPS* with module vibration revealed clear synergistic effects (Fig. 4). The most effective configurations were Sp.2 and Sp.4 combined with high vibration (2.54 cm), which increased the initial permeate flux by 337.5% and 333.8%, respectively, relative to the initial flux of the control configuration without spacer and vibration. The corresponding initial fluxes were 203.10 and 201.35 L m^{-2} h^{-1}, respectively, compared with 46.42 L m^{-2} h^{-1} for the control. The flux enhancement observed in the present study is in agreement with the findings of [15], who reported that a 3D-printed membrane-integrated spacer with a gyroid geometry enhanced permeate flux by approximately 152% and 181% compared with a commercial spacer after 30 and 120 min of ultrafiltration, respectively. Their results also highlighted the influence of spacer geometry on membrane hydrodynamics and fouling behavior, supporting the role of appropriately designed spacer structures in enhancing membrane filtration performance. This outcome aligns with the respective design principles of these two spacers: the tapering profile of Sp.2 already concentrates shear stress at the membrane surface under static conditions, and the addition of high-frequency vibration appears to compound this effect, further intensifying local turbulence beyond what either mechanism could achieve independently. Similarly, the reinforced junctions of Sp.4 not only preserved the flow-distribution advantages of the branched geometry under vibration-induced stress but also allowed the spacer to sustain effective shear generation throughout the vibration cycle, rather than losing structural integrity or flow control over time. Filtering times and flux decay rates were comparable across these two top-performing combinations, suggesting that once shear intensity surpasses a certain threshold, further gains in flux stability become less dependent on the specific geometric mechanism involved. While low-vibration scenarios combined with *3DPS* also outperformed the control, they did not reach the performance level achieved under high-vibration conditions. For instance, Sp.1 under low vibration (0.635 cm) exhibited an initial flux 23% lower than that of Sp.2 under high vibration, indicating that vibration intensity, rather than spacer geometry alone, plays a decisive role in determining the upper limit of achievable flux enhancement.

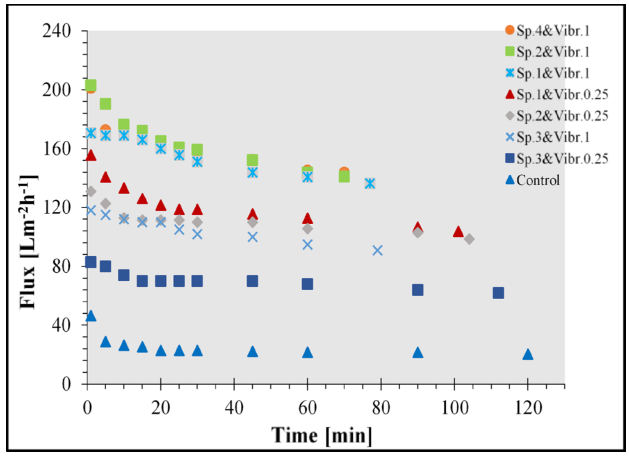

Fig. 4 Time-dependent permeate flux profiles for combined *3DPS* and module vibration configurations, illustrating the synergistic effect of spacer geometry and vibration intensity relative to the control

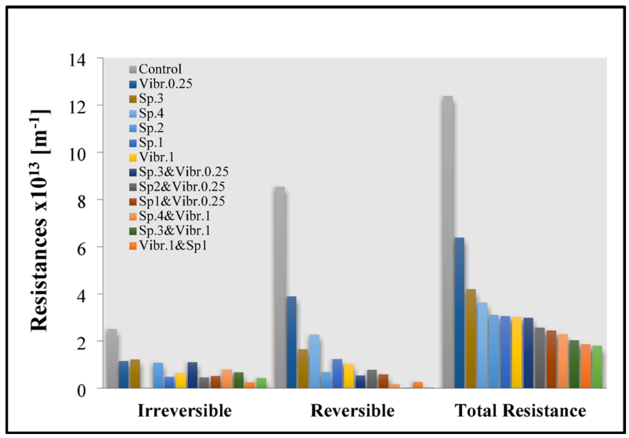

Fig. 5 Distribution of irreversible, reversible, and total membrane resistance for the control and *3DPS*-integrated configurations under low and high vibration conditions

3.2 Membrane resistances analysis

Using Eqs. (3–6), the resistance-in-series model was applied to evaluate the contribution of each resistance component to overall filtration performance. As shown in Fig. 5, all tested conditions led to a significant reduction in total resistance compared with the control. Low vibration alone decreased total resistance by approximately 50%, while either high vibration or the use of individual 3DPS designs achieved average reductions closer to 70%. Combining high vibration with spacer integration produced the most substantial decreases overall, ranging from approximately 82% to 86% depending on geometry, with Sp.1 and Sp.2 reaching the highest reductions (≥85%); Sp.2 yielded the lowest overall resistance among all tested configurations. This result is consistent with the conical geometry's capacity to concentrate flow acceleration and shear stress at the membrane surface, an effect that appears to be further amplified once high-frequency vibration is superimposed on the already shear-intensive flow field it generates. With respect to the individual resistance fractions, both high vibration and *3DPS* integration were effective in suppressing reversible resistance, nearly eliminating the contribution of the gel layer in most configurations. This suggests that the loosely bound cake layer, being the most readily disrupted fouling component, is highly susceptible to the additional shear generated by either mechanism, regardless of the specific spacer geometry involved. The behavior of irreversible resistance, however, proved more geometry-dependent. Sp.4 alone reduced irreversible resistance to nearly zero, an outcome consistent with its reinforced branched structure, which distributes flow evenly across the membrane while minimizing the localized stagnation zones typically responsible for deeper, more persistent fouling. Notably, when combined with high vibration, the irreversible resistance of Sp.4 increased rather than decreased further, suggesting that the added vibrational energy may disrupt the uniform flow distribution that underlies its standalone effectiveness, potentially redistributing foulants into a more compact and less reversible form. Sp.2, by contrast, exhibited a genuinely synergistic response to vibration, achieving an additional ~55% reduction in irreversible resistance when the two mechanisms were combined; its flow-accelerating, shear-concentrating geometry appears inherently compatible with, rather than disrupted by, the additional shear input from vibration.

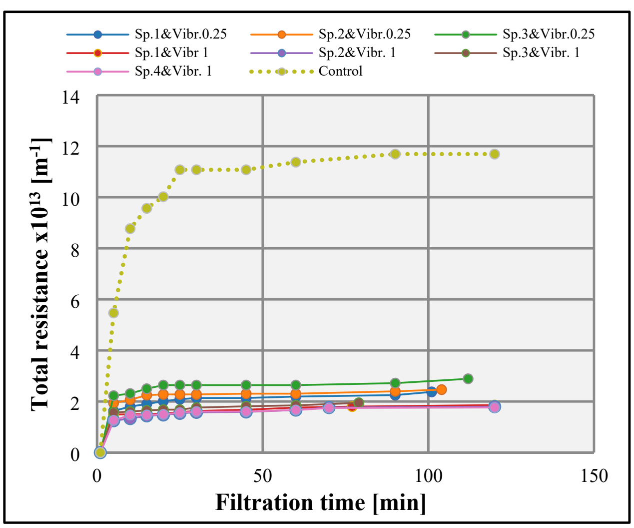

Fig. 6 Real-time evolution of total membrane resistance during filtration for the combined 3DPS with vibration configurations, with the control shown as a dotted reference line

To complement the end-point R_T distribution presented in Fig. 5, 6 illustrates the time-dependent evolution of R_T throughout filtration for all combined spacer with vibration configurations. R_T was calculated at each sampling interval, allowing its development to be evaluated throughout the filtration period rather than only at the endpoint. Configurations with shorter filtration durations correspond to experiments terminated when the *VRR* reached 2. The control exhibited a continuous increase in R_T, from 5.5×10^{13} m^{-1} at 1 min to 12.4×10^{13} m^{-1} at 120 min. In contrast, all combined spacer with vibration configurations substantially suppressed R_T development from the early stages of filtration and maintained considerably lower R_T throughout the operating period. Under low vibration, Sp.1 and Sp.2 showed similar R_T reductions, with reductions of approximately 80 and 79%, respectively, relative to the control. Sp.3 achieved a comparatively lower reduction of approximately 76%, indicating a weaker R_T reductions effect at the lower vibration intensity. Under high vibration, Sp.2 provided the greatest R_T reduction, reaching approximately 85% relative to the control. Sp.1 and Sp.3 followed closely, with reductions of approximately 85% and 84%, respectively, while Sp.4 achieved an approximately 81% reduction. Overall, these results demonstrate that combining 3DPS with module vibration effectively suppresses the development of membrane R_T from the early stages of filtration and maintains this effect throughout the investigated operating period. The extent of R_T reductions depended on both spacer geometry and vibration intensity, with higher vibration generally providing greater suppression of R_T development.

3.3 Retention of the organic matter

To evaluate organic matter retention, *COD* was measured in the feed, permeate, and concentrate streams (Fig. 7). Compared with the control, most treatments demonstrated modest improvements in *COD* retention, ranging from approximately 5–14%. The highest retention values were achieved with the combined application of spacers and vibration, particularly Sp.2 under low vibration, which reached nearly 67% retention; this result suggests that even at reduced vibration intensity, the flow-accelerating geometry of Sp.2 is sufficient to limit the passage of organic solutes without requiring the additional shear input of high vibration. By contrast, Sp.3 combined with vibration exhibited marginally lower performance than the control, with retention values 2–4% below baseline, a result consistent

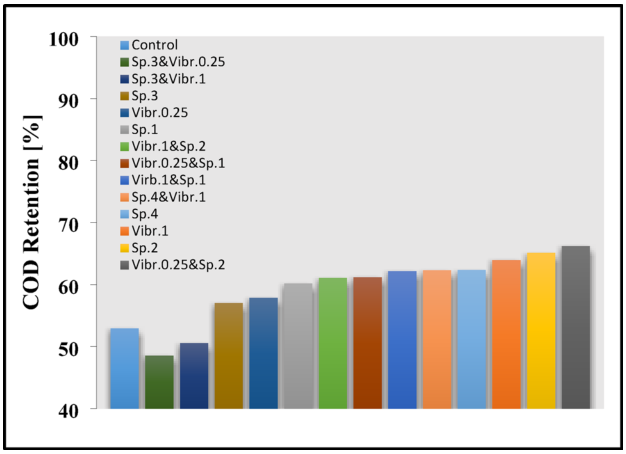

Fig. 7 *COD* retention for the control and *3DPS*/vibration configurations, individually and in combination, arranged in ascending order of retention performance

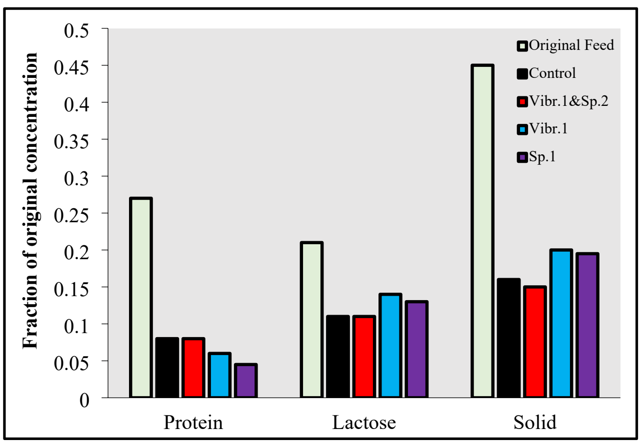

Fig. 8 Protein, lactose, and total solids content of permeates relative to the original feed concentration, measured by Bentley 150 infrared spectroscopy

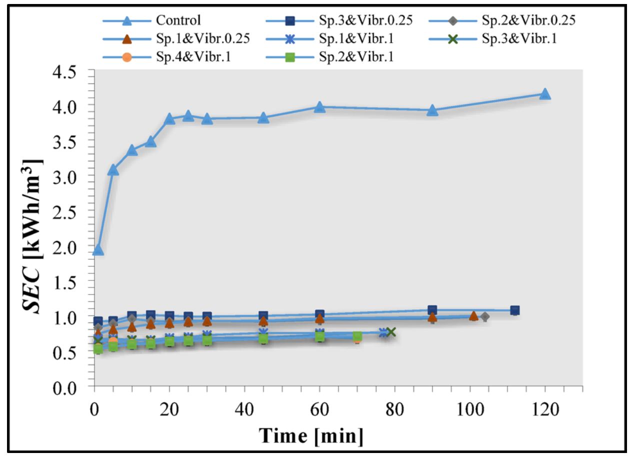

Fig. 9 Specific energy consumption as a function of time for the control and combined experiments

with its comparatively lower shear-generating capacity, which may allow a slightly greater fraction of organic matter to permeate rather than remain concentrated at the membrane surface. Overall, these variations indicate that while mechanical interventions such as vibration and spacer integration can modestly enhance *COD* retention, their primary influence lies in flux enhancement and resistance reduction rather than in substantially improving organic matter removal.

3.4 Effect of 3DPS and vibration on permeate composition

Compositional analyses were carried out to evaluate the effects of vibration, *3DPS*, and their combined application on protein, lactose, and total solids retention in the permeate (Fig. 8). Compared with the original feed, the control achieved substantial reductions, lowering protein by ~70%, lactose by ~50%, and total solids by ~67%. High vibration further enhanced protein removal, reducing it by ~77%, while lactose decreased by ~55%, with total solids behaving similarly to the control. The *3DPS* configuration (Sp.1) yielded the most pronounced protein reduction (~83%), consistent with the cylindrical spacer's capacity to generate widespread turbulence and concentrate protein micelles and larger organic aggregates at the membrane surface; lactose retention, however, remained comparable to other conditions at ~60%, approximately 13% lower than the control, reflecting the smaller molecular size and higher solubility of lactose, which limit its exclusion regardless of the shear conditions applied. For total solids, Sp.1 provided slightly higher reductions (~60%) than the control. Interestingly, the combined high-vibration and Sp.2 configuration was less effective for protein and lactose retention, producing values nearly identical to the control, though it achieved a modest improvement (~6%) in total solids reduction. This outcome contrasts with the synergistic behavior observed for flux and resistance under the same combination, suggesting that the intense shear generated by pairing high vibration with the conical spacer's flow-accelerating geometry may promote greater turbulence and mixing near the membrane surface, which, while beneficial for limiting cake-layer formation, could simultaneously reduce the residence time of protein and lactose molecules at the membrane, allowing a larger fraction to pass into the permeate.

3.5 Specific energy consumption under spacer and vibration conditions

SEC profiles for all tested conditions are presented in Fig. 9. The control exhibited the highest energy demand, increasing steadily to values exceeding 4.0 kWh·m^{-3}, reflecting the progressive decline in permeate flux as fouling accumulated over the filtration run. In contrast, all vibration-assisted and spacer-integrated configurations demonstrated substantially lower *SEC* values, consistent with their ability to sustain higher flux and lower resistance throughout the process. Low-vibration conditions stabilized between 0.7–0.9 $kWh \cdot m^{-3}$, while high vibration further reduced *SEC* to approximately 0.5–0.6 $kWh \cdot m^{-3}$, corresponding to energy savings of 58% and 71%, respectively, relative to the control. Notably, the combined high-vibration and spacer configurations yielded the most efficient overall performance, with only minimal increases in *SEC* over time, a trend that mirrors the flux stability and low resistance values observed for these same configurations. Among them, Sp.2 and Sp.4 under high vibration provided the lowest energy demand, reaching a final *SEC* of ~0.63 $kWh\ m^{-3}$, representing an ~85% reduction relative to the control. This outcome reinforces the earlier resistance and flux results: because both spacers sustain elevated flux with comparatively little decline over time, the energy required per unit volume of permeate produced remains low even as the vibration motor continues to consume power.

3.6 SEM and AFM analysis of membrane surface fouling

SEM was performed to evaluate the surface morphology of the pristine, fouled, and spacer-assisted membranes operated within the cross-flow system (Fig. 10). For each sample, two representative regions (denoted as areas 1 and 2) were examined to account for spatial variability across the membrane surface. The pristine membrane exhibited a relatively smooth and homogeneous morphology, with no visible deposits or pore blockage, confirming its structural integrity prior to filtration. In contrast, the fouled membrane displayed extensive surface coverage by irregular, compact agglomerates, indicating the formation of a dense cake layer. These deposits partially or completely obstructed membrane pores, resulting in increased surface roughness and heterogeneity, features characteristic of severe fouling and consistent with the pronounced permeate flux decline and marked increase in total resistance observed during filtration. By contrast, the membrane operated in the presence of the spacer exhibited a considerably cleaner surface than the fouled membrane, with only a limited number of loosely attached deposits and large portions of the surface remaining exposed. The absence of a continuous cake layer suggests that the spacer enhanced local hydrodynamic conditions and increased shear stress at the membrane surface, thereby limiting foulant accumulation and preventing the dense, pore-blocking layer observed under uncontrolled fouling. This improved surface morphology is consistent with the reduced flux decline and lower the total resistance values recorded in the spacer-assisted filtration experiments, reinforcing the link between the shear-enhancing action of the spacer geometry and the mitigation of surface fouling observed at the macroscopic scale.

AFM was employed to investigate the surface topography of the *PES* membrane under different operating conditions and to relate these morphological changes to the observed filtration performance (Fig. 11). The pristine membrane exhibited a smooth, homogeneous surface, reflected in its low roughness values (Ra = 4.01 nm, Rq = 5.07 nm), consistent with its high initial permeate flux and low intrinsic membrane resistance. In contrast, the membrane operated without vibration or spacer showed a pronounced increase in surface roughness (Ra = 21.47 nm, Rq = 28.47 nm), roughly a fivefold increase over the pristine membrane. The corresponding *AFM* images revealed irregular peaks and valleys indicative of foulant deposition and cake layer formation, consistent with the severe permeate flux decline and substantial increase in total resistance observed under these conditions. When a spacer was introduced, the membrane surface exhibited a markedly lower roughness (Ra = 11.22 nm, Rq = 14.88 nm), roughly half that of the fouled membrane, alongside a more uniform topography. This improvement is consistent with enhanced local hydrodynamic conditions and increased shear-driven mass transfer near the membrane surface, which limited foulant deposition and prevented the formation of a thick, continuous cake layer, in agreement with the improved permeate flux and reduced total resistance observed experimentally. Similarly, applying vibration alone reduced surface roughness (Ra = 10.04 nm, Rq = 13.12 nm) to a level comparable to, and marginally lower than, the spacer-assisted membrane, with a more evenly distributed surface topography and reduced peak heights. This indicates that vibration-induced shear forces were similarly effective in limiting foulant accumulation and partially disrupting the developing cake layer, consistent with the mitigated flux decline and lower total resistance values measured under vibrated conditions. Notably, the kurtosis values (Rku) followed an inverse trend relative to Ra and Rq, increasing from 4.41 for the pristine membrane to 6.28 for the spacer-assisted membrane and 4.75 for the vibrated membrane, both exceeding the fouled membrane's value of 4.62. Since Rku values above 3 indicate a surface dominated by sharp, narrow peaks rather than broad, rounded ones, this suggests that although both spacer and vibration treatments substantially reduced overall surface roughness, the residual foulant deposits remaining on these surfaces were more discrete and peak-like in nature, rather than forming the broad, continuous agglomerates characteristic of the heavily fouled membrane. This finer, less continuous deposition pattern is consistent with the effective

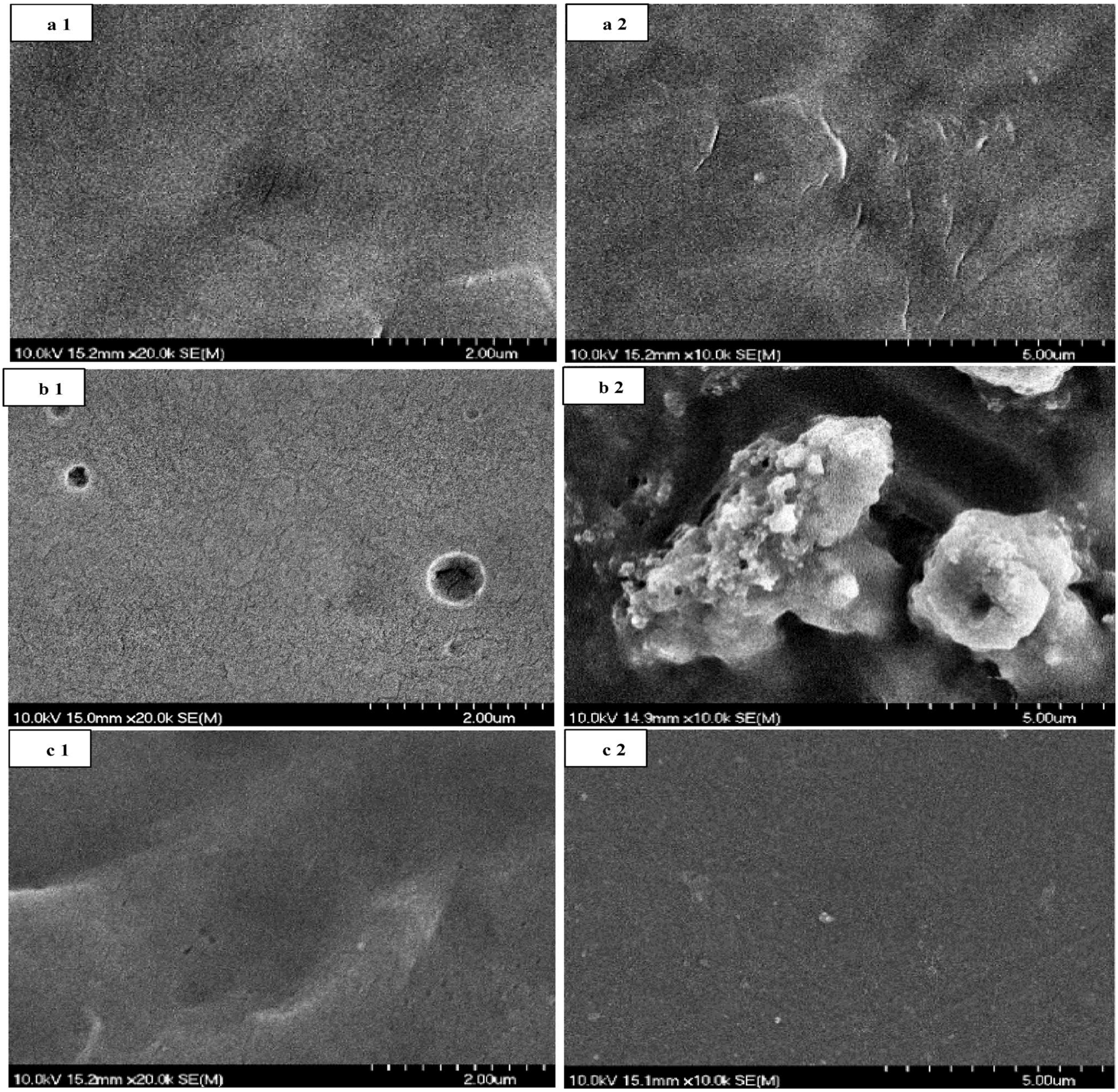

Fig. 10 SEM micrographs illustrating the surface morphology of the membranes: **a1**–**a2** pristine membrane, **b1**–**b2** fouled membrane after filtration, and **c1**–**c2** membrane operated with spacer

disruption of cake-layer formation by both treatments, even where some residual surface roughness persisted.

4 Conclusion

This study systematically evaluated the integration of four *3DPS* designs, cylindrical, conical, branched, and reinforced branched, into a cross-flow ultrafiltration system, both independently and in combination with module vibration. Key performance indicators, including permeate flux, *COD* retention, total resistance, and specific energy consumption, were measured to assess the fouling-mitigation potential of each configuration. The results demonstrated that incorporating *3DPS* into the module, particularly the conical spacer, combined with high-intensity module vibration increased permeate flux by up to 300% relative to the control. COD retention showed only modest improvement compared with the substantial increase in permeate flux, increasing from 52.95% for the control to a maximum of 66.21% for Sp.2 under low vibration, while total resistance decreased across all tested combined spacer with vibration

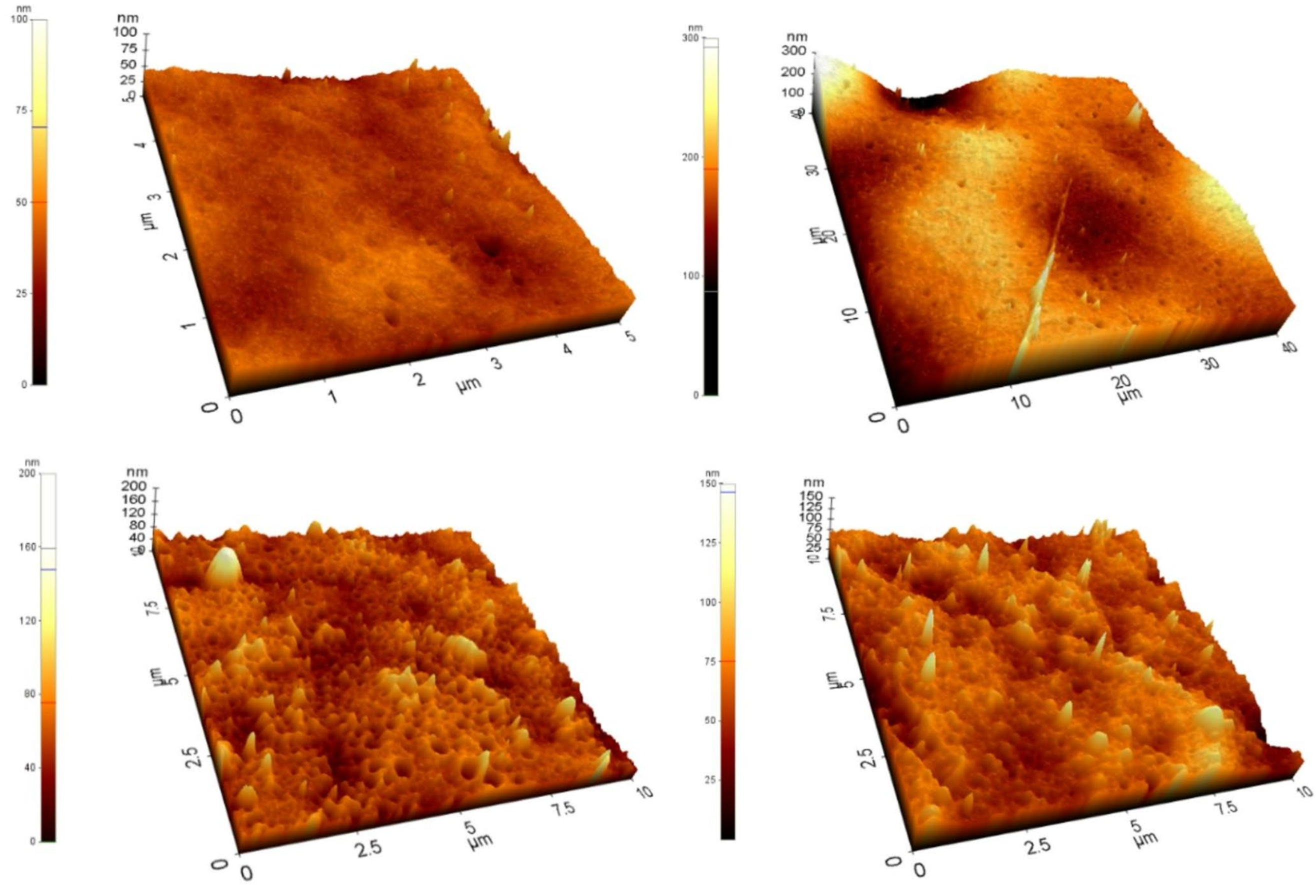

Fig. 11 *AFM* topographical images showing the surface morphology of ultrafiltration PES membranes under different conditions: **a** pristine membrane, **b** fouled membrane, **c** membrane operated with spacer assistance, and **d** membrane operated under vibration

scenarios by approximately 76% to 85% relative to the control, with the most pronounced reduction observed when the conical spacer was operated under high vibration. Specific energy consumption analysis further confirmed that combining *3DPS* with vibration represented the most energy-efficient operating strategy, low vibration operation reduced *SEC* by approximately 58%, while high vibration operation achieved an approximately 71% reduction relative to the control. The greatest improvement was obtained when high vibration was combined with *3DPS*, with Sp.2 and Sp.4 reaching a final *SEC* of approximately 0.63 kWh m^{-3}, corresponding to an approximately 85% reduction relative to the control. Among all tested conditions, the conical and reinforced branched spacer configurations operated under high vibration provided the best overall balance of flux enhancement, resistance reduction, and energy efficiency. *SEM* and *AFM* surface analyses provided direct morphological confirmation of these fouling-mitigation effects. While severely fouled membranes exhibited dense cake-layer formation, pore blockage, and pronounced surface roughness, both spacer- and vibration-assisted membranes retained considerably cleaner, smoother, and more homogeneous surfaces, with roughness values markedly lower than those of the fouled membrane. The corresponding surface kurtosis values further indicated that residual deposits on the spacer- and vibration-assisted membranes were more discrete and finely distributed, rather than forming the broad, continuous agglomerates characteristic of uncontrolled fouling. Taken together, these findings confirm that the synergistic combination of optimized spacer geometry and module vibration offers an effective, energy-conscious strategy for mitigating membrane fouling and sustaining long-term ultrafiltration performance in dairy wastewater treatment.

Acknowledgements Acknowledgments This study was supported by the 142414 FK and 2022-1.2.6-TÉT-IPARI-TR-2022-00011 grants from the National Research, Development and Innovation Office (NKFI), Hungary. Aws N. Al-Tayawi acknowledges the financial support provided through the Ministry of Culture and Innovation Research Fellowship Program, funded by the National Fund for Research, Development and Innovation (grant number EKÖP-24-3-SZTE-476). We also thank the University of Szeged Open Access Fund (8901) for support.

Author contribution Author Contributions Aws N. Al-Tayawi (first and corresponding author): conceptualization, methodology, software, investigation, formal analysis, writing-original draft, and funding acquisition; Noor Al-Hammadi: data curation, methodology, formal analysis, writing—original draft and validation; Omar K. Mohialdeen: data curation, software, methodology, formal analysis, validation, writing—reviewing and editing; Imre Vajk Fazekas and Bence Szilveszter Virág: conceptualization, methodology, data curation, writing-original draft, resources, software, and validation; Judit Kopniczky: conceptualization, methodology, software, investigation, formal analysis, writing—reviewing and editing; Tamás Gyulavári: methodology, software, investigation, formal analysis, writing—reviewing and editing; Zsuzsanna László: methodology, data curation, writing—original draft, and resources. Szabolcs Kertész: methodology, conceptualization, investigation, funding acquisition, resources, supervision, writing—review and editing.

Funding Open access funding provided by University of Szeged. This work was financially supported by the National Research, Development and Innovation Office (NKFI), Hungary (142414 FK and 2022–1.2.6-TÉT-IPARI-TR-2022-00011 grants), the National Fund for Research, Development and Innovation through the Ministry of Culture and Innovation Research Fellowship Program (grant number EKÖP-26-4-SZTE−478) and the University of Szeged Open Access Fund (8901).

Data availability No datasets were generated or analysed during the current study.

Declarations

Conflict of interest The author(s) declare no conflict of interest.

References

1. Abid HS, Johnson DJ, Hashaikeh R, Hilal N (2017) A review of efforts to reduce membrane fouling by control of feed spacer characteristics. Desalination 420:384–402
2. Abobeh S, Abdelsalam MM, El BMA (2025) An overview study on water desalination, hybrid RO systems, and how to utilize artificial intelligence with the system. Water Conserv Sci Eng 10:85
3. Cabrera-Castillo EH, Thomas N, Al-Ketan O et al (2019) 3D printed spacers for organic fouling mitigation in membrane distillation. J Memb Sci 581:331–343. https://doi.org/10.1016/j.memsci.2019.03.040
4. Cheng M, Xie X, Schmitz P, Fillaudeau L (2021) Extensive review about industrial and laboratory dynamic filtration modules: scientific production, configurations and performances. Sep Purif Technol 265:118293
5. Chevarin C, Wang X, Bouyer D et al (2023) CFD-guided patterning of tubular ceramic membrane surface by stereolithography: optimizing morphology at the mesoscale for improved hydrodynamic control of membrane fouling. J Memb Sci 672:121435
6. Cui Z, Ma J, Zhang Y et al (2026) A review on membrane biofouling during downtime of pharmaceutical water treatment equipment: risks, mechanisms, and control strategies. J Microbiol Methods. https://doi.org/10.1016/j.mimet.2026.107415
7. Duan H, Peng C, Liu Y et al (2024) Spatial distribution, risk assessment and sources of heavy metals in roadside soils exposed to the Zhengzhou-Kaifeng intercity railway in Huanghuai Plain, China. Soil Sediment Contam Int J 33(8):1463–1484
8. Foorginezhad S, Zerafat MM, Ismail AF, Goh PS (2025) Emerging membrane technologies for sustainable water treatment: a review on recent advances. Environ Sci Adv 4:530–570
9. Gáspár I, Neczpál R (2020) Testing of 3D printed turbulence promoters for membrane filtration. Period Polytech Chem Eng 64:371–376
10. Goon GSS, Labban O, Foo ZH, Zhao X (2021) Deformation-induced cleaning of organically fouled membranes: fundamentals and techno-economic assessment for spiral-wound membranes. J Membr Sci 626:119169
11. Ibrahim Y, Hilal N (2023) Enhancing ultrafiltration membrane permeability and antifouling performance through surface patterning with features resembling feed spacers. npj Clean Water 6:60. https://doi.org/10.1038/s41545-023-00277-3
12. Ibrar I, Naji O, Sharif AO et al (2019) A review of fouling mechanisms, control strategies and real-time fouling monitoring techniques in forward osmosis. Water 11:695. https://doi.org/10.3390/w11040695
13. Imbrogno A, Schäfer AI (2019) Comparative study of nanofiltration membrane characterization devices of different dimension and configuration (cross flow and dead end). J Membr Sci 585:67–80
14. Kertész S (2023) Evaluation of Vibratory Shear-enhanced Processing Module-integrated Three-dimensional Printed Spacers for Enhanced Wastewater Ultrafiltration. Water Environ Res. https://doi.org/10.1002/wer.10912
15. Khalil A, Francis L, Hashaikeh R, Hilal N (2022) 3D Printed Membrane-integrated Spacers for Enhanced Antifouling in Ultrafiltration. J Appl Polym Sci. https://doi.org/10.1002/app.53019
16. Konieczny K, Sąkol D, Płonka J et al (2009) Coagulation—ultrafiltration system for river water treatment. Desalination 240:151–159
17. Lee J, Kim D, Kim S et al (2025) Comprehensive evaluation of a pilot-scale semiconductor wastewater reuse process using ultrafiltration and two-stage reverse osmosis for securing intake water resource in ultrapure water production. Desalination 613:119115
18. Lin W, Wang Q, Liu Z et al (2024) Improved hydrodynamic properties and enhanced resistance to particle deposition and membrane fouling by millimeter-scale patterned membranes. J Memb Sci 700:122709. https://doi.org/10.1016/j.memsci.2024.122709
19. Liu W, Livingston JL, Wang L et al (2024) Pressure-driven membrane desalination. Nat Rev Methods Prim 4:10
20. Ltaief S, Matéos A, Forestier A et al (2025) Sustainable protein recovery and wastewater valorization in shrimp processing by ultrafiltration. Foods 14:2044
21. Mardal F, Ali A, Mehmood A et al (2025) From characterisation to strategy: a comprehensive review of fouling in dairy ultrafiltration and microfiltration. Food Bioprod Process 151:312–326
22. Méthot-Hains S, Benoit S, Bouchard C et al (2016) Effect of transmembrane pressure control on energy efficiency during skim milk concentration by ultrafiltration at 10 and 50°C. J Dairy Sci 99:8655–8664. https://doi.org/10.3168/jds.2016-11504
23. Niu C, Li X, Dai R, Wang Z (2022) Artificial intelligence-incorporated membrane fouling prediction for membrane-based processes in the past 20 years: a critical review. Water Res. https://doi.org/10.1016/j.watres.2022.118299

24. Osman AI, Chen Z, Elgarahy AM et al (2024) Membrane technology for energy saving: principles, techniques, applications, challenges, and prospects. Adv Energy Sustain Res 5:2400011
25. Park S, Dal Jeong Y, Lee JH et al (2021) 3D printed honeycomb-shaped feed channel spacer for membrane fouling mitigation in nanofiltration. J Memb Sci 620:118665
26. Pasquet PL, Villain-Gambier M, Trébouet D (2023) Productivity, selectivity performances and fouling control of brewery wastewater micro-ultrafiltration through operation optimization and membrane screening. J Water Process Eng 53:103815
27. Rajendran DS, Devi EG, Subikshaa VS et al (2025) Recent advances in various cleaning strategies to control membrane fouling: a comprehensive review. Clean Technol Environ Policy 27:649–664
28. Shen J, Yang M, Mao Z, Xing J (2025) A new linear growth theoretical model of protein reversible fouling layer in protein wastewater ultrafiltration: fouling mechanism prediction for different proteins and pressures. Water Res. https://doi.org/10.1016/j.watres.2025.124866
29. Siagian UWR, Khoiruddin K, Wardani AK et al (2021) High-performance ultrafiltration membrane: recent progress and its application for wastewater treatment. Curr Pollut Rep 7:448–462
30. Soliman M, Eljack F, Kazi M-K et al (2021) Treatment technologies for cooling water blowdown: a critical review. Sustainability 14:376
31. Sutrisna PD, Kurnia KA, Siagian UWR et al (2022) Membrane fouling and fouling mitigation in oil–water separation: a review. J Environ Chem Eng. https://doi.org/10.1016/j.jece.2022.107532
32. Tan YZ, Mao Z, Zhang Y et al (2019) Enhancing fouling mitigation of submerged flat-sheet membranes by vibrating 3D-spacers. Sep Purif Technol 215:70–80. https://doi.org/10.1016/j.seppur.2018.12.085
33. Wang Q, Lin W, Chou S et al (2023) Patterned membranes for improving hydrodynamic properties and mitigating membrane fouling in water treatment: a review. Water Res 236:119943
34. Wisniewski CM, Laurio MVO, Slater CS, Savelski MJ (2020) Environmental and process assessment of a vibratory nanofiltration system for the recovery of water from soluble coffee manufacturing waste. Environ Prog Sustain Energy 39:e13425
35. Xia S, Liu M, Yu H, Zou D (2023) Pressure–driven membrane filtration technology for terminal control of organic DBPs: a review. Sci Total Environ 904:166751
36. Zouboulis AI, Peleka EN, Ntolia A (2019) Treatment of tannery wastewater with vibratory shear-enhanced processing membrane filtration. Separations 6:20

Publisher's Note Springer Nature remains neutral with regard to jurisdictional claims in published maps and institutional affiliations.